Gate-tunable heavy fermions in a moiré Kondo lattice

https://doi.org/10.1038/s41586-023-05800-7

Received: 29 October 2022

Accepted: 6 February 2023

Wenjin Zhao[1], Bowen Shen[2], Zui Tao[2], Zhongdong Han[3], Kaifei Kang[2], Kenji Watanabe[4], Takashi Taniguchi[4], Kin Fai Mak[1,2,3] ✉ & Jie Shan[1,2,3] ✉

The Kondo lattice—a matrix of local magnetic moments coupled through spin-exchange interactions to itinerant conduction electrons—is a prototype of strongly correlated quantum matter[1–4]. Usually, Kondo lattices are realized in intermetallic compounds containing lanthanide or actinide[1,2]. The complex electronic structure and limited tunability of both the electron density and exchange interactions in these bulk materials pose considerable challenges to studying Kondo lattice physics. Here we report the realization of a synthetic Kondo lattice in AB-stacked $MoTe_2/WSe_2$ moiré bilayers, in which the $MoTe_2$ layer is tuned to a Mott insulating state, supporting a triangular moiré lattice of local moments, and the WSe_2 layer is doped with itinerant conduction carriers. We observe heavy fermions with a large Fermi surface below the Kondo temperature. We also observe the destruction of the heavy fermions by an external magnetic field with an abrupt decrease in the Fermi surface size and quasi-particle mass. We further demonstrate widely and continuously gate-tunable Kondo temperatures through either the itinerant carrier density or the Kondo interaction. Our study opens the possibility of in situ access to the phase diagram of the Kondo lattice with exotic quantum criticalities in a single device based on semiconductor moiré materials[2–9].

Moiré materials provide a highly tunable platform to explore strongly correlated electron phenomena[5,6,10,11]. A series of correlated insulating, magnetic and superconducting states has emerged as a result of the flat electronic bands induced by the moiré superlattices[5,6,10–12]. In particular, a Mott insulator with localized magnetic moments has been realized in semiconductor moiré materials at half-filling of the moiré band[13–15]. The strong electronic interactions open a Mott gap with a fully filled Hubbard band. Coupling itinerant electrons to the lattice of local moments through exchange interaction has been proposed as a route to realizing a Kondo lattice[16–21].

Here we experimentally demonstrate the realization of a moiré Kondo lattice in AB-stacked (60°-aligned) $MoTe_2/WSe_2$ bilayers with hole doping. These bilayers form a triangular moiré lattice with a period of about 5 nm, corresponding to a moiré density of $n_M \approx 5\times10^{12}$ cm^{-2}, as a result of the 7% mismatch between the $MoTe_2$ and WSe_2 lattices[22–24]. The Wannier orbitals of the topmost $MoTe_2$ and WSe_2 valence bands are centred on two distinct high-symmetry stacking sites of the moiré lattice. Together, they form a honeycomb lattice[25–28]. The moiré potential is substantially stronger at the Mo site than at the W site (see section 'Estimate of the bandwidths' in the Methods for further discussion). Hence, the first $MoTe_2$ moiré band is relatively flat and the first WSe_2 moiré band is dispersive. The holes in the $MoTe_2$ layer can be localized by interactions, whereas the holes in the WSe_2 layer remain itinerant. This is supported by density functional calculations[25] as well as the experimental results discussed below.

In dual-gated devices (Fig. 1a), the two gate voltages can independently tune the total electrostatic doping density, ν (in units of n_M), in the bilayer and the electric field, E, perpendicular to the bilayer. The electric field tunes the interlayer potential difference or band alignment[22]. We consider a scenario in which the first WSe_2 moiré band is slightly below the $MoTe_2$ moiré band. The interlayer hopping integral, $t_\perp$ (Fig. 1b), remains weak because, to a good approximation, the two bands have opposite spins for the same valley and the interlayer hopping is nearly spin-forbidden[24,25]. The system has been shown to undergo topological phase transitions at both $\nu = 1$ and $\nu = 2$ upon band inversion[22,24]. Particularly, at $\nu = 1$, it is a Mott (or charge transfer) insulator before the band inversion and a quantum anomalous Hall insulator after the band inversion[22,28].

A simple Kondo lattice away from the mixed-valence regime[29] can be seen before the band inversion. It corresponds to the shaded region of the (ν, E) phase diagram (Fig. 1c, top). For a full phase diagram, see Extended Data Fig. 1. The total doping density is $\nu = 1 + x$ with the hole density in the $MoTe_2$ layer (ν_{Mo}) fixed at 1 and in the WSe_2 layer (ν_W) at $x > 0$. This is achievable for a range of electric fields, for which the dispersive WSe_2 moiré band is inside the $MoTe_2$ Mott gap, and the Fermi level cuts through the WSe_2 band[16,17] (Fig. 1c, inset). The electric-field span of the region, ΔE, provides a measure of the Mott gap, $U = d\Delta E$, where d is the interlayer dipole moment of the bilayer[30,31]. Furthermore, because the Fermi energy scales linearly with density for massive electrons in two dimensions, the boundaries of the Kondo lattice region shift linearly with x.

The possibility of separating the local moments and conduction holes into two different layers provides remarkable gate tunability of

---

[1]Kavli Institute at Cornell for Nanoscale Science, Cornell University, Ithaca, NY, USA. [2]School of Applied and Engineering Physics, Cornell University, Ithaca, NY, USA. [3]Laboratory of Atomic and Solid State Physics, Cornell University, Ithaca, NY, USA. [4]National Institute for Materials Science, Tsukuba, Japan. ✉e-mail: kinfai.mak@cornell.edu; jie.shan@cornell.edu

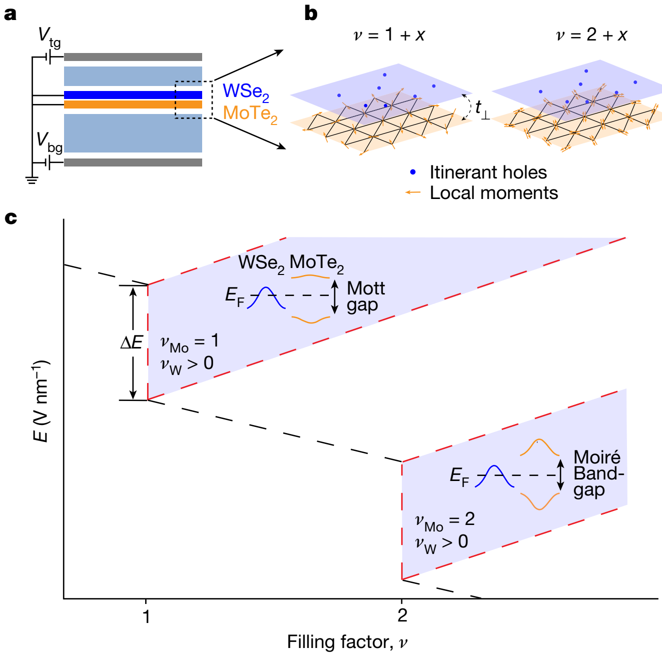

Fig. 1 | Moiré Kondo lattice in AB-stacked MoTe$_2$/WSe$_2$. a, Schematic side view of a dual-gated Hall bar device of AB-stacked MoTe$_2$/WSe$_2$. **b**, Left, schematic of a moiré Kondo lattice. The MoTe$_2$ layer is filled with one hole per moiré site ($\nu_{Mo} = 1$) and the WSe$_2$ layer hosts the itinerant holes ($\nu_W = x$). Here $t_\perp$ denotes the interlayer hoping. Right, the corresponding scenario when the MoTe$_2$ layer is filled with two holes per moiré site ($\nu_{Mo} = 2$) with anti-aligned spins; no Kondo lattice physics is expected in this case. **c**, The (ν, E) phase diagram with regions defined by different fillings in MoTe$_2$ and WSe$_2$. Kondo lattice physics is realized in region II ($\nu_{Mo} = 1$ and $\nu_W = x$); region III ($\nu_{Mo} = 2$ and $\nu_W = x$) provides a control experiment. Insets, the moiré band structure corresponding to regions II and III. The Fermi level is located in between the MoTe$_2$ Hubbard bands in region II and the MoTe$_2$ moiré bands in region III, and it goes through the WSe$_2$ moiré band. The electric-field span ΔE (arrow) is directly proportional to the Mott gap in region II or the moiré bandgap in region III. The WSe$_2$ layer is charge-neutral below the black dashed lines in the phase diagram.

the Kondo effect[16,17,19]. The Kondo coupling, J_K, between a conduction hole and local moment is estimated to be approximately $2t_\perp^2\left(\frac{1}{\Delta}+\frac{1}{U-\Delta}\right)$ by considering an interlayer (anti-ferromagnetic) super-exchange interaction, where Δ is the charge transfer gap[16,17]. Bringing the WSe$_2$ band close to resonance with either Hubbard band by the electric field can significantly enhance J_K. When the Kondo coupling effect dominates, the conduction holes hybridize with (or screen) the local moments to produce a large Fermi surface with heavy quasi-particle masses. The onset temperature for Kondo screening increases with J_K and the conduction hole density.

A moiré Kondo lattice

We performed magneto-transport and optical spectroscopy measurements to identify the Kondo lattice region. Details about the device fabrication and measurements are provided in the Methods. Figure 2a shows the longitudinal resistance, R_{xx}, as a function of (ν, E) under an out-of-plane magnetic field $B = 13.6$ T at temperature $T = 1.6$ K. The doping density and electric field were determined from the gate voltages using the parallel-plate capacitor model, and the density was independently calibrated by the quantum oscillation measurements. The grey regions could not be accessed in the current device structure because of either large sample or contact resistance or limited accessible gate voltages. Quantum oscillations (stripes) could be observed in many regions of the phase diagram, indicating a Fermi-liquid behaviour.

For $\nu = 1 + x$, we identify a region with pronounced vertical stripes (region II). In this region, the Landau levels do not disperse with E—that is, the electric field does not affect the Fermi surface. This is consistent with the Fermi level located inside the Mott gap ($\nu_{Mo} = 1$ and $\nu_W = x$). The level degeneracy is also consistent with the formation of

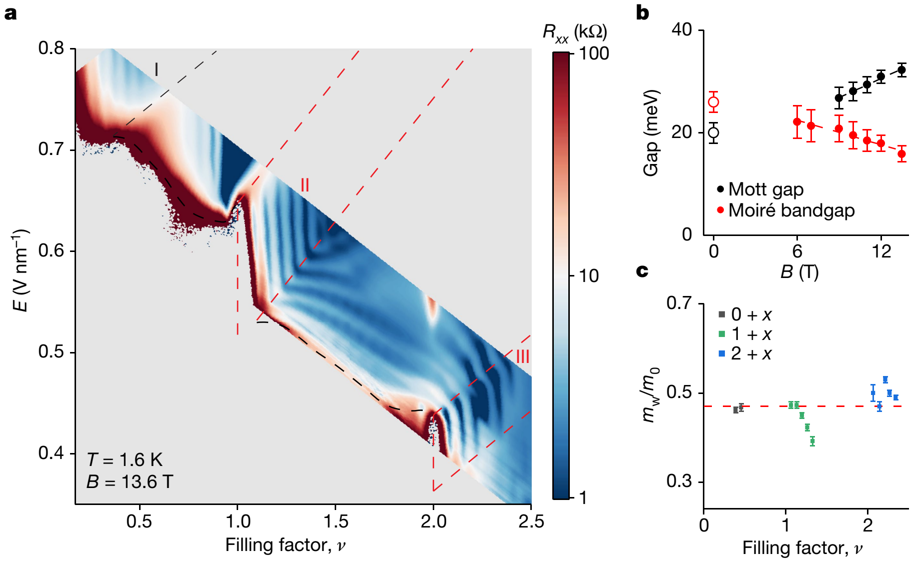

Fig. 2 | Electrostatics phase diagram. a, Dependence of R_{xx} on the total filling factor ν and the out-of-plane electric field E at $B = 13.6$ T and $T = 1.6$ K. The dashed lines mark the phase boundaries between the different regions in the electrostatics phase diagram corresponding to Fig. 1c and Extended Data Fig. 1. The red dashed lines mark the boundaries for regions II and III. **b**, Magnetic-field dependence of the Mott gap and the moiré bandgap extracted from the electric-field span in regions II and III, respectively. The zero magnetic field data (empty dots) are obtained from optical measurements (Extended Data Fig. 3). The dashed lines are guides to the eye. **c**, Filling-factor dependence of the WSe$_2$ itinerant hole mass (normalized by the free electron mass m_0) extracted from the temperature-dependent quantum oscillations (Extended Data Fig. 4) in region I ($\nu = \nu_{Mo} + \nu_W = 0 + x$), region II ($\nu = 1 + x$) and region III ($\nu = 2 + x$). Data points with different colours correspond to different regions. The dashed line denotes the average (or mean) hole mass. The drop in mass near $\nu = 1$ is probably caused by a systematic error from background subtractions. The background in region II shows a much stronger temperature dependence than the other regions. Error bars denote the standard deviation from data fitting.

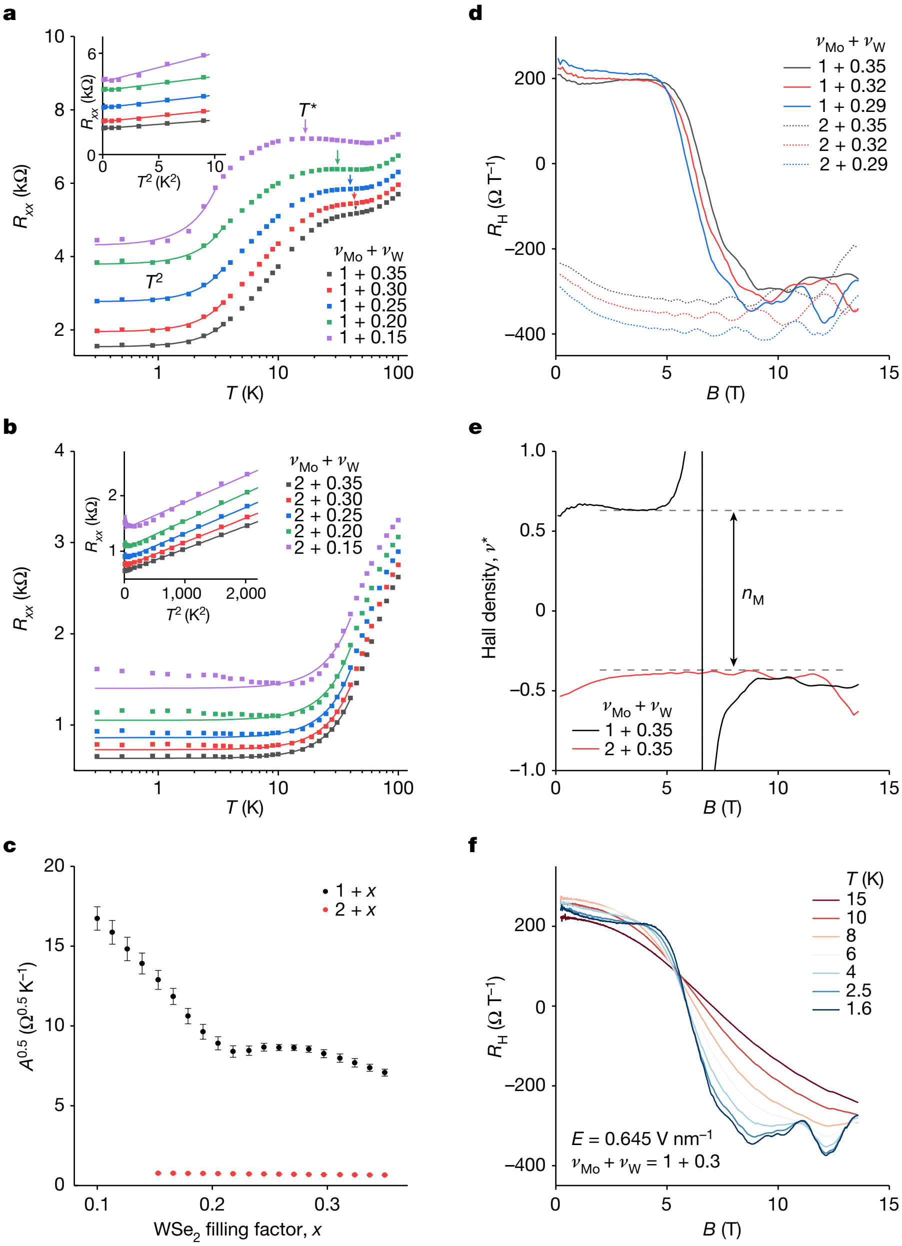

Fig. 3 | Emergence of heavy fermions and magnetic destruction of Kondo singlets. a,b, Temperature-dependent R_{xx} at varying doping densities for $\nu = 1 + x$ (**a**) and $\nu = 2 + x$ (**b**). The solid lines are the best fits to the quadratic temperature dependence at low temperatures. The arrows mark the temperature T^*. The insets show the scaling of R_{xx} with T^2. **c**, Extracted doping dependence of the coefficient $A^{0.5}$ for both $\nu = 1 + x$ (black) and $\nu = 2 + x$ (red). Error bars denote the standard deviation from data fitting. **d**, Magnetic-field dependence of the Hall coefficient R_H at $T = 1.6$ K for both $\nu = 1 + x$ (solid curves) and $\nu = 2 + x$ (dotted curves). A sharp change in R_H at the critical magnetic field is observed only for $\nu = 1 + x$, whereas at $\nu = 2 + x$ it is weakly field dependent. **e**, The corresponding magnetic-field dependence of the Hall density ν^* for $\nu = 1 + 0.35$ and $\nu = 2 + 0.35$. The arrow indicates a change in the Hall density by the moiré density n_M. **f**, Magnetic-field dependence of R_H at $\nu = 1 + 0.3$ and varying temperatures.

spin-valley-polarized Landau levels only in the WSe$_2$ layer. By contrast, in the region with smaller electric fields beneath region II, the vertical stripes turn into diagonal ones and a second set of weaker stripes emerges and intersects the first set. The prominent quantum oscillations arise from the WSe$_2$ layer, whereas the weaker ones arise from the MoTe$_2$ layer, because the latter has a heavier mass and lower mobility. The Fermi level cuts through bands of both layers. The stripes disperse with E because the field varies the relative alignment of the Landau levels from two different layers. We estimate the Mott gap of region II to be about 32 meV from its electric-field span, assuming the interlayer dipole moment $d \approx e \times 0.26$ nm (from optical measurements, where e denotes the elementary charge)[23].

Pronounced vertical stripes can also be identified in two other regions: region I with $\upsilon = x$ and region III with $\upsilon = 2 + x$. Similarly, these vertical stripes correspond to quantum oscillations in the WSe$_2$ layer with density x. The Fermi level is located in an energy gap of the MoTe$_2$ layer —specifically, in the large semiconductor bandgap in region I ($\upsilon_{Mo} = 0$) and the gap between the first and second moiré bands in region III ($\upsilon_{Mo} = 2$). The full extent of region I is beyond the accessible gate voltages. We estimate the moiré bandgap from the electric-field span of region III to be about 16 meV assuming the same interlayer dipole moment d. Both the Mott and moiré bandgaps depend on the magnetic field owing to the Zeeman effect (Fig. 2b, Methods and Extended Data Fig. 2). The zero-field Mott and moiré bandgaps

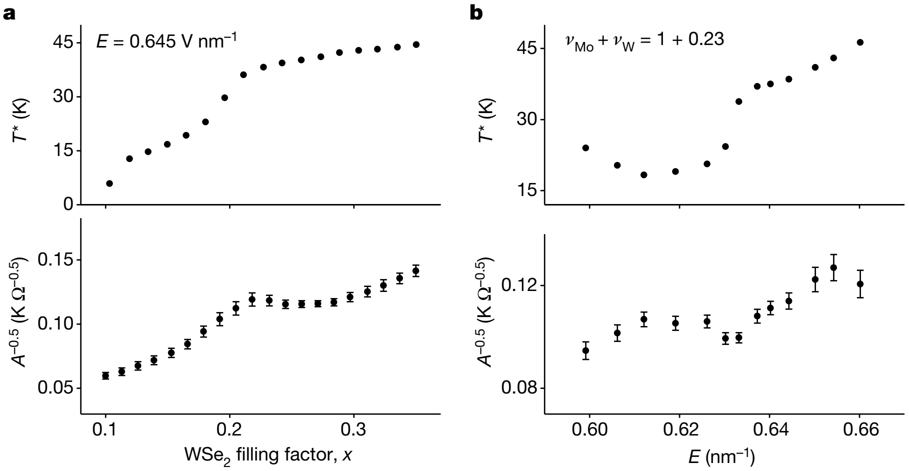

Fig. 4 | Gate-tunable moiré Kondo physics. a, Extracted doping dependence of T^* (top) and $A^{-0.5}$ (bottom) at a fixed electric field ($E = 0.645$ V nm^{-1}) for $\nu = 1 + x$. The two quantities show similar dependences. **b**, Extracted electric-field dependence of T^* (top) and $A^{-0.5}$ (bottom) at a fixed filling factor ($\nu = 1 + 0.23$). We observed an asymmetric dependence with respect to the $MoTe_2$ lower ($E \approx 0.66$ V nm^{-1}) and upper ($E \approx 0.6$ V nm^{-1}) Hubbard bands. Error bars denote the standard deviation from data fitting.

(20 and 26 meV, respectively) are inferred from the layer-resolved exciton optical response (Extended Data Fig. 3).

We determine the quasi-particle mass of WSe_2 from the temperature dependence of the quantum oscillations (Fig. 2c and Extended Data Fig. 4). At 13.6 T, the value is around $0.5m_0$ in all three regions (m_0 denoting the electron mass). It is slightly larger than the hole mass in monolayer WSe_2 (approximately $0.45m_0$)[32]. This result supports a dispersive WSe_2 band and weak moiré potential at the W sites.

The simultaneous existence of a sizeable Mott gap in $MoTe_2$, which supports a triangular lattice of local moments and of itinerant holes in WSe_2 in region II, provides the key ingredients for a Kondo lattice. Next we determine whether a heavy-fermion liquid emerges. Because the Kondo effect was not expected in region III, in which the first $MoTe_2$ moiré band is fully filled with two holes of opposite spin, we use region III as a control experiment (Fig. 1).

Emergence of heavy fermions

Figure 3a,b shows the temperature dependence of the resistance under zero magnetic field in region II ($E = 0.645$ V nm^{-1}) and region III ($E = 0.45$ V nm^{-1}), respectively. Different curves correspond to different doping densities; the same colour denotes the same hole density in the WSe_2 layer. In both regions, R_{xx} decreases with increasing x and shows a T^2 dependence at low temperatures (Fig. 3a,b (insets)). R_{xx} deviates from the T^2 dependence below 10 K for $x \lesssim 0.15$ in region III, the origin of this effect is currently unknown. In region II, there is a characteristic temperature T^*, below which resistance drops significantly, and T^* increases with x. No resistance peak or onset of significant drop in resistance is observed in region III in the studied temperature range.

The T^2 dependence of R_{xx} at low temperatures is a characteristic of a Landau Fermi liquid. We fit the dependence using $R_{xx} = R_0 + AT^2$, where R_0 is the residual resistance limited by impurity scattering, and $A^{0.5}$ is linearly proportional to the quasi-particle mass in the Fermi-liquid theory[33]. The doping dependence of $A^{0.5}$ is shown in Fig. 3c. The value in region II is more than an order of magnitude larger than that in region III, and the enhancement ratio further increases from approximately 10 to 20 as x decreases from 0.35 to 0.1. The large enhancement indicates the emergence of heavy fermions in region II.

We measure the size of the Fermi surface by measuring the Hall resistance, R_{xy}. Figure 3d shows the magnetic-field dependence of the Hall coefficient, $R_H = R_{xy}/B$, for representative doping densities in regions II and III. The corresponding result for R_{xx} is included in Extended Data Fig. 5. In region III, R_H weakly depends on the field up to 14 T. Oscillatory features appear above approximately 4 T from the formation of Landau levels. Conversely in region II, R_H has an opposite sign at low fields. It shows an abrupt change, including a sign switch around a critical field, $B_c \approx 6$ T; and above B_c, it reaches a similar value to that in region III for the same x. The oscillatory features are not observable below B_c and become visible immediately above B_c.

For a given doping density, the magnetoresistance at varying temperatures follows Kohler's scaling (Extended Data Fig. 6). Therefore, we assume a single charge-carrier type and evaluated the Hall density, υ^* (in units of n_M), from the Hall coefficient as $1/(eR_Hn_M)$ for $x = 0.35$ in Fig. 3e as an example. In region III, we obtain $\upsilon^* \approx -x$, which indicates a hole Fermi surface with density x. This is expected because the first $MoTe_2$ moiré band is fully filled with two holes, and the Fermi level cuts through the WSe_2 moiré band inside the $MoTe_2$ moiré bandgap. The Hall density is also consistent with the value extracted from quantum oscillations. In region II, below B_c, we obtain $\nu^* \approx 1 - x$. This indicates an electron Fermi surface with density $1 - x$, which is equivalent to a hole density of $1 + x$ because the band degeneracy is 2. This result indicates that the local moments in the $MoTe_2$ layer are hybridized with the conduction holes in the WSe_2 layer to form a large-hole Fermi surface. This surface, which is observed in combination with the quasi-particle mass enhancement, supports the realization of a Kondo lattice in region II[4]. We use the characteristic temperature T^*, below which R_{xx} decreases significantly, to measure the Kondo temperature. The Kondo temperature is much smaller than the Fermi temperature of the itinerant hole .

Magnetic destruction of heavy fermions

The Hall measurement in region II shows that the large Fermi surface with hole density $1 + x$ is reduced to a small Fermi surface with hole density x when a magnetic field above B_c is applied. The reduction in the size of the Fermi surface is also correlated with the emergence of a light-fermion liquid, as evidenced by the immediate appearance of quantum oscillations. We determine the mass of the quasi-particle from the temperature dependence of the quantum oscillations to be around $0.5m_0$, which is comparable with the value in regions I and III (Fig. 2c).

Magnetic destruction of heavy fermions is possible when the Zeeman energy exceeds the Kondo temperature, below which the Kondo singlets emerge[4,34,35]. We estimate the critical Zeeman energy ($g\mu_B B_c$ around 3 meV at $x \approx 0.3$) using the hole g factor ($g \approx 10$) in monolayer transition metal dichalcogenides[36] (where μ_B is the Bohr magneton).

It agrees well with the corresponding Kondo temperature ($T^* \approx 40$ K). Magnetic destruction of heavy fermions could be a meta-magnetic phase transition or a smooth crossover[4,37]. The significant narrowing of the R_H sign-change region with decreasing temperature (Fig. 3f) indicates a meta-magnetic phase transition[38]. Meta-magnetic transitions from a Kondo-singlet paramagnet to a spin-polarized paramagnet have been reported in rare-earth heavy-fermion compounds[34]. Future experiments that correlate the Hall and magnetization measurements are required to understand the nature of the transition in moiré Kondo lattices.

Gate-tunable coherent Kondo effect

Finally, we demonstrate continuous gate tuning of the Kondo effect. We study the temperature dependence of the resistance and extract the Kondo temperature T^* and the parameter $A^{-0.5}$ in region II (Fig. 4 and Extended Data Fig. 7). We show one cut along $E = 0.645$ V nm^{-1} (Fig. 4a) and another cut along $x = 0.23$ (Fig. 4b). The Kondo temperature (Fig. 4a,b (top)) can be widely tuned by both doping and electric field. The inverse of the mass enhancement, $A^{-0.5}$ (Fig. 4a,b (bottom)), largely follows T^* as expected[39] and the product, $A(T^*)^2$, stays near the resistance quantum[40]. Increasing the doping density is expected to strengthen the Kondo effect because there are more conduction holes to screen the local moments[16,17,39]. This is consistent with the observed dependence of T^* on x. However, we observe a stronger enhancement of the Kondo effect when the WSe_2 band is close to the $MoTe_2$ lower Hubbard band ($E \approx 0.66$ V nm^{-1}) than the upper band ($E \approx 0.6$ V nm^{-1}). This apparent disagreement with the simple estimate of the Kondo coupling on the basis of super-exchange interaction[16] shows the presence of asymmetry in the two Hubbard bands (Methods) and indicates that possibly more interaction mechanisms are required to describe our system.

In conclusion, we have realized a Kondo lattice in AB-stacked $MoTe_2$/WSe_2 moiré bilayers when the WSe_2 layer is doped with itinerant holes and the $MoTe_2$ layer stayed in a Mott insulating state. We have also observed a heavy-fermion liquid with a large Fermi surface. Our work shows a highly gate-tunable Kondo effect. It provides opportunities to study the gate-controlled Kondo destruction transition by extending the Kondo temperature further down to 0 K—for instance, by reducing the doping density in higher-quality devices or the interaction effect in bilayers with small twist angles[16].

Online content

Any methods, additional references, Nature Portfolio reporting summaries, source data, extended data, supplementary information, acknowledgements, peer review information; details of author contributions and competing interests; and statements of data and code availability are available at https://doi.org/10.1038/s41586-023-05800-7.

1. Stewart, G. R. Heavy-fermion systems. *Rev. Mod. Phys.* **56**, 755–787 (1984).
2. Kirchner, S. et al. Colloquium: heavy-electron quantum criticality and single-particle spectroscopy. *Rev. Mod. Phys.* **92**, 011002 (2020).
3. Paschen, S. & Si, Q. Quantum phases driven by strong correlations. *Nat. Rev. Phys.* **3**, 9–26 (2021).
4. Coleman, P. Heavy fermions and the Kondo lattice: a 21st century perspective. Preprint at https://arxiv.org/abs/1509.05769 (2015).
5. Kennes, D. M. et al. Moiré heterostructures as a condensed-matter quantum simulator. *Nat. Phys.* **17**, 155–163 (2021).
6. Mak, K. F. & Shan, J. Semiconductor moiré materials. *Nat. Nanotechnol.* **17**, 686–695 (2022).
7. Maksimovic, N. et al. Evidence for a delocalization quantum phase transition without symmetry breaking in $CeCoIn_5$. *Science* **375**, 76–81 (2022).
8. Senthil, T., Vojta, M. & Sachdev, S. Weak magnetism and non-Fermi liquids near heavy-fermion critical points. *Phys. Rev. B* **69**, 035111 (2004).
9. Vojta, M. Orbital-selective Mott transitions: heavy fermions and beyond. *J. Low Temp. Phys.* **161**, 203–232 (2010).
10. Andrei, E. Y. et al. The marvels of moiré materials. *Nat. Rev. Mater.* **6**, 201–206 (2021).
11. Andrei, E. Y. & MacDonald, A. H. Graphene bilayers with a twist. *Nat. Mater.* **19**, 1265–1275 (2020).
12. Cao, Y. et al. Unconventional superconductivity in magic-angle graphene superlattices. *Nature* **556**, 43–50 (2018).
13. Tang, Y. et al. Simulation of Hubbard model physics in WSe_2/WS_2 moiré superlattices. *Nature* **579**, 353–358 (2020).
14. Regan, E. C. et al. Mott and generalized Wigner crystal states in WSe_2/WS_2 moiré superlattices. *Nature* **579**, 359–363 (2020).
15. Wu, F., Lovorn, T., Tutuc, E. & Macdonald, A. H. Hubbard model physics in transition metal dichalcogenide moiré bands. *Phys. Rev. Lett.* **121**, 026402 (2018).
16. Kumar, A., Hu, N. C., Macdonald, A. H. & Potter, A. C. Gate-tunable heavy fermion quantum criticality in a moiré Kondo lattice. *Phys. Rev. B* **106**, L041116 (2022).
17. Guerci, D. et al. Chiral Kondo lattice in doped $MoTe_2$/WSe_2 bilayers. Preprint at https://arxiv.org/abs/2207.06476 (2022).
18. Ramires, A. & Lado, J. L. Emulating heavy fermions in twisted trilayer graphene. *Phys. Rev. Lett.* **127**, 026401 (2021).
19. Dalal, A. & Ruhman, J. Orbitally selective Mott phase in electron-doped twisted transition metal-dichalcogenides: a possible realization of the Kondo lattice model. *Phys. Rev. Res.* **3**, 043173 (2021).
20. Song, Z.-D. & Bernevig, B. A. Magic-angle twisted bilayer graphene as a topological heavy fermion problem. *Phys. Rev. Lett.* **129**, 047601 (2022).
21. Vaňo, V. et al. Artificial heavy fermions in a van der Waals heterostructure. *Nature* **599**, 582–586 (2021).
22. Li, T. et al. Quantum anomalous Hall effect from intertwined moiré bands. *Nature* **600**, 641–646 (2021).
23. Li, T. et al. Continuous Mott transition in semiconductor moiré superlattices. *Nature* **597**, 350–354 (2021).
24. Zhao, W. et al. Realization of the Haldane Chern insulator in a moiré lattice. Preprint at https://arxiv.org/abs/2207.02312 (2022).
25. Zhang, Y., Devakul, T. & Fu, L. Spin-textured Chern bands in AB-stacked transition metal dichalcogenide bilayers. *Proc. Natl Acad. Sci. USA* **118**, e2112673118 (2021).
26. Rademaker, L. Spin-orbit coupling in transition metal dichalcogenide heterobilayer flat bands. *Phys. Rev. B* **105**, 195428 (2022).
27. Pan, H., Xie, M., Wu, F. & Sarma, S. D. Topological phases in AB-stacked $MoTe_2$/WSe_2: Z_2 topological insulators, Chern insulators, and topological charge density waves. *Phys. Rev. Lett.* **129**, 056804 (2022).
28. Devakul, T. & Fu, L. Quantum anomalous Hall effect from inverted charge transfer gap. *Phys. Rev. X* **12**, 021031 (2022).
29. Varma, C. M. Mixed-valence compounds. *Rev. Mod. Phys.* **48**, 219–238 (1976).
30. Gu, J. et al. Dipolar excitonic insulator in a moiré lattice. *Nat. Phys.* **18**, 395–400 (2022).
31. Zhang, Z. et al. Correlated interlayer exciton insulator in heterostructures of monolayer WSe_2 and moiré WS_2/WSe_2. *Nat. Phys.* **18**, 1214–1220 (2022).
32. Fallahazad, B. et al. Shubnikov–de Haas oscillations of high-mobility holes in monolayer and bilayer WSe_2: Landau level degeneracy, effective mass, and negative compressibility. *Phys. Rev. Lett.* **116**, 086601 (2016).
33. Kadowaki, K. & Woods, S. B. Universal relationship of the resistivity and specific heat in heavy-fermion compounds. *Solid State Comm.* **58**, 507–509 (1986).
34. Kitagawa, S. et al. Metamagnetic behavior and Kondo breakdown in heavy-fermion CeFePO. *Phys. Rev. Lett.* **107**, 277002 (2011).
35. Gegenwart, P., Si, Q. & Steglich, F. Quantum criticality in heavy-fermion metals. *Nat. Phys.* **4**, 186–197 (2008).
36. Mak, K. F., Xiao, D. & Shan, J. Light–valley interactions in 2D semiconductors. *Nat. Photon.* **12**, 451–460 (2018).
37. Löhneysen, H. V., Rosch, A., Vojta, M. & Wölfle, P. Fermi-liquid instabilities at magnetic quantum phase transitions. *Rev. Mod. Phys.* **79**, 1015–1075 (2007).
38. Paschen, S. et al. Hall-effect evolution across a heavy-fermion quantum critical point. *Nature* **432**, 881–885 (2004).
39. Burdin, S., Georges, A. & Grempel, D. R. Coherence scale of the Kondo lattice. *Phys. Rev. Lett.* **85**, 1048–1051 (2000).
40. Sarma, S. D. & Liao, Y. Know the enemy: 2D Fermi liquids. *Ann. Phys.* **435**, 168495 (2021).

Methods

Device fabrication

We fabricated dual-gated $MoTe_2$/WSe_2 devices using a layer-by-layer dry-transfer technique as previously reported[22,23,41]. We aligned the $MoTe_2$ and WSe_2 monolayers by first determining the crystallographic orientations of each monolayer using the optical second-harmonic generation technique[13,14]. The bilayers aligned at 0° and 60° were then sorted according to their distinct electric-field dependence of the longitudinal resistance at $\nu = 1$ (refs. [22,23]). $MoTe_2$ is air-sensitive and was handled in a glovebox with O_2 and H_2O concentrations below 1 ppm. We first fabricated the bottom gates, consisting of hexagonal boron nitride (hBN) of approximately 10 nm thickness and a few layers of graphite on silicon substrates with pre-patterned Ti/Au electrodes. The polycarbonate residue from the dry-transfer process was removed in chloroform for 2 h. We deposited 5-nm Pt contacts on hBN by standard electron-beam lithography and evaporation, followed by another step of electron-beam lithography and metallization to form a bilayer of 5-nm Ti and 40-nm Au to connect the thin Pt contacts on hBN to pre-patterned electrodes. We cleaned the device surface after lift-off using an atomic force microscope in contact mode. For the top gates, we chose a relatively thin hBN layer (around 4 nm) to achieve high breakdown electric fields of the order of 1 V nm^{-1}. We also chose a narrow top gate electrode made of graphite, which defines the region of interest in the Hall bar geometry. The results in the main text were obtained from device 1. All results were reproduced in device 2 (Extended Data Fig. 8).

Electrical measurements

Electrical measurements were performed in a closed-cycle ^{4}He cryostat with a ^{3}He insert (Oxford TeslatronPT). The measurements were performed under magnetic fields up to 14 T and temperature down to 300 mK. The standard low-frequency (10–20 Hz) lock-in technique was used to measure the sample resistance at low bias (0.2–1 mV). A voltage pre-amplifier with 100-MΩ impedance was used to measure the sample resistance up to about 10 MΩ. The longitudinal and transverse voltage drops and the source drain current were recorded. Finite longitudinal–transverse coupling occurs in our devices. We used a standard procedure to obtain the longitudinal and Hall resistances by symmetrizing $\frac{R_{xx}(B) + R_{xx}(-B)}{2}$ and anti-symmetrizing $\frac{R_{xy}(B) - R_{xy}(-B)}{2}$ the measured R_{xx} and R_{xy} values under positive and negative magnetic fields, respectively.

Estimate of the bandwidths

The density functional theory calculations and our experiment show that the moiré potential is substantially stronger for holes in the $MoTe_2$ layer than in the WSe_2 layer[25]. A plausible explanation is that lattice corrugations and strain-induced band energy shift contribute notably to the moiré potential in AB-stacked $MoTe_2$/WSe_2 bilayers. The Young modulus of WSe_2 is about 1.7 times that of $MoTe_2$, and lattice corrugations under lattice reconstruction in WSe_2 are much smaller[42,43].

We estimate the upper limit of the width of the first WSe_2 moiré band from the doping density and density of states. Assuming a parabolic band of mass m_W, the density of states is $\frac{\mathrm{d}n}{\mathrm{d}E} = \frac{m_W}{\pi\hbar^2}$, where $\hbar$ is the reduced Planck constant. The total density of the first moiré band is $2n_M \approx 1 \times 10^{13}\ cm^{-2}$. We obtain an upper bound for the dispersive WSe_2 bandwidth of about 48 meV using $m_W \approx 0.5m_0$ obtained from the experiment.

The $MoTe_2$ lower Hubbard bandwidth can be estimated by $d\Delta E$, where d is the interlayer dipole moment, which is around 0.26 e× nm (ref. [23]), and ΔE is the electric-field difference when the WSe_2 valence band edge is aligned with the maximum and minimum of the lower Hubbard band. These two fields are $E \approx 0.7$ V nm^{-1} (corresponding to the band inversion point with $\nu_W = \nu_{Mo} = 0$) and $E \approx 0.65$ V nm^{-1} (with $\nu_W = 0$ and $\nu_{Mo} = 1$) as shown in Fig. 2a and Extended Data Fig. 2. We estimate that lower Hubbard bandwidth is 13 meV. Similarly, we estimate that upper Hubbard bandwidth is 26 meV.

Determination of the Mott, moiré band and charge transfer gaps

In the main text, we described how the Mott and moiré bandgaps were determined from the (ν, E) map of R_{xx} at 13.6 T from the electric-field span of regions II and III, respectively. We performed the same measurements under varying magnetic fields. Extended Data Fig. 2 shows the result under several representative magnetic fields. The quantum oscillations are no longer discernable for $B < 6$ T in region II because of the formation of heavy fermions, but persist down to 4 T in region III. Figure 2b summarizes the Mott and moiré bandgaps that are dependent on the magnetic field. The zero-field values were obtained from the layer-resolved exciton optical response (Extended Data Fig. 3), which is sensitive to charge doping. In region III, the magnetic field lifts the spin degeneracy of the moiré bands and continuously reduces the moiré bandgap by the Zeeman effect. By contrast, in region II, the field first polarizes the local moments and then increases the Mott gap above saturation by introducing an additional Zeeman splitting between the Hubbard bands[13].

The determination of the charge transfer gap is shown in Extended Data Fig. 9. It is given by the product of the interlayer dipole moment d and the electric-field difference ΔE between the threshold electric field for band inversion and the applied electric field. For example, the charge transfer gap is estimated to be around 2 meV for the data in Fig. 3. It is continuously tuned in Fig. 4 by the electric field.

Estimate of the heavy-fermion mass

The magnetic destruction of the Kondo singlets at rather small critical magnetic fields (around 6 T) prevents us from directly determining the quasi-particle mass of the heavy fermions from the temperature-dependent quantum oscillations. Quantum oscillations cannot be observed below 6 T for the heavy fermions because of the large quasi-particle mass and the presence of disorder. Therefore, we can only estimate the heavy-fermion mass by assuming that the ratio of the quasi-particle mass in regions II and III equals the ratio of $A^{0.5}$ based on the Kadowaki–Woods scaling[33]. Given the measured WSe_2 quasi-particle mass m_W (around $0.5m_0$) and the ratio of $A^{0.5}$ (10–20 for varying x) (Figs. 2c and 3c), the heavy-fermion mass is estimated to be 5 to 10 times m_0.

Determination of the Kondo temperature

The Kondo temperature T^* is a crossover temperature scale, below which coherent charge transport in the lattice of Kondo singlets develops[2]. The sample resistance significantly drops below T^*. In our experiment, we observe a peak or kink in the temperature-dependent resistance (Fig. 3a and Extended Data Fig. 7). Because of the broad feature of a crossover, the numerical accuracy for T^* is limited. The crossover temperature T^* was extracted as the first minimum of $|\mathrm{d}R_{xx}/\mathrm{d}T|$ (Extended Data Fig. 10), which corresponds to the resistance peak temperature or the temperature below which the resistance decreases significantly.

Data availability

Source data are provided with this paper. All other data are available from the corresponding authors upon reasonable request.

41. Wang, L. et al. One-dimensional electrical contact to a two-dimensional material. *Science* **342**, 614–617 (2013).
42. Zhang, R., Koutsos, V. & Cheung, R. Elastic properties of suspended multilayer WSe_2. *Appl. Phys. Lett.* **108**, 042104 (2016).
43. Sun, Y. et al. Elastic properties and fracture behaviors of biaxially deformed, polymorphic $MoTe_2$. *Nano Lett.* **19**, 761–769 (2019).

Acknowledgements We thank L. Fu, D. Guerci, A. Millis, A. Georges, A. Rubio, S. Todadri, A. Kumar, A. Potter, D. Chowdhury and Y. Zhang for discussions. This work was supported by the Air Force Office of Scientific Research under award number FA9550-19-1-0390 (transport measurements), the National Science Foundation (Platform for the Accelerated Realization, Analysis, and Discovery of Interface Materials) under cooperative agreement nos. DMR-2039380 (sample and device fabrication) and DMR-2004451 (optical measurements) and the US Department of Energy, Office of Science, Basic Energy Sciences, under award number DE-SC0019481 (analysis). This work is also funded in part by the Gordon and Betty Moore Foundation. The growth of the hBN crystals was supported by the Elemental Strategy Initiative of MEXT, Japan, and CREST (JPMJCR15F3), JST. We used the Cornell Center for Materials Research Shared Facilities supported through the NSF MRSEC programme (DMR-1719875) and of the Cornell NanoScale Facility, an NNCI member supported by NSF grant NNCI-2025233. We also acknowledge support from the David and Lucille Packard Fellowship (K.F.M.) and the Kavli Postdoctoral Fellowship (W.Z.).

Author contributions W.Z. and B.S. fabricated the devices. W.Z. and B.S. performed the electrical transport measurements and analysed the data with the help of Z.H.; K.K., Z.T. and W.Z. carried out the optical measurements; K.W. and T.T. grew the bulk hBN crystals; W.Z., K.F.M. and J.S. designed the scientific objectives and oversaw the project. All authors discussed the results and commented on the manuscript.

Competing interests The authors declare no competing interests.

Additional information

Supplementary information The online version contains supplementary material available at https://doi.org/10.1038/s41586-023-05800-7.
Correspondence and requests for materials should be addressed to Kin Fai Mak or Jie Shan.
Peer review information *Nature* thanks Lihong Bao and the other, anonymous, reviewer(s) for their contribution to the peer review of this work. Peer reviewer reports are available.
Reprints and permissions information is available at http://www.nature.com/reprints.

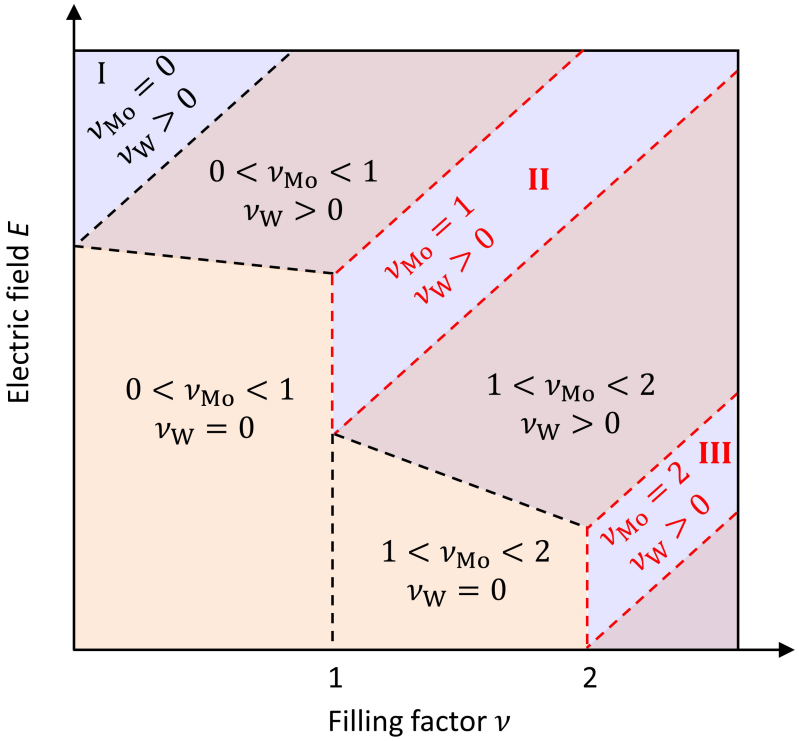

Extended Data Fig. 1 | Schematic electrostatics phase diagram. The (ν, E) phase diagram with regions defined by different fillings in $MoTe_2$ and WSe_2. Kondo lattice physics is realized in region II ($\nu_{\mathrm{Mo}} = 1$ and $\nu_{\mathrm{W}} = x$); region III ($\nu_{\mathrm{Mo}} = 2$ and $\nu_{\mathrm{W}} = x$) provides a control experiment. In addition to regions I, II and III discussed in the main text, we can also identify regions with $\nu_{\mathrm{W}} = 0$ and $0 < \nu_{\mathrm{Mo}} < 2$, where WSe_2 is charge-neutral and only $MoTe_2$ is hole-doped, as well as regions where holes are shared between the two TMD layers ($\nu_{\mathrm{W}} > 0$ and $0 < \nu_{\mathrm{Mo}} < 1$ and $\nu_{\mathrm{W}} > 0$ and $1 < \nu_{\mathrm{Mo}} < 2$).

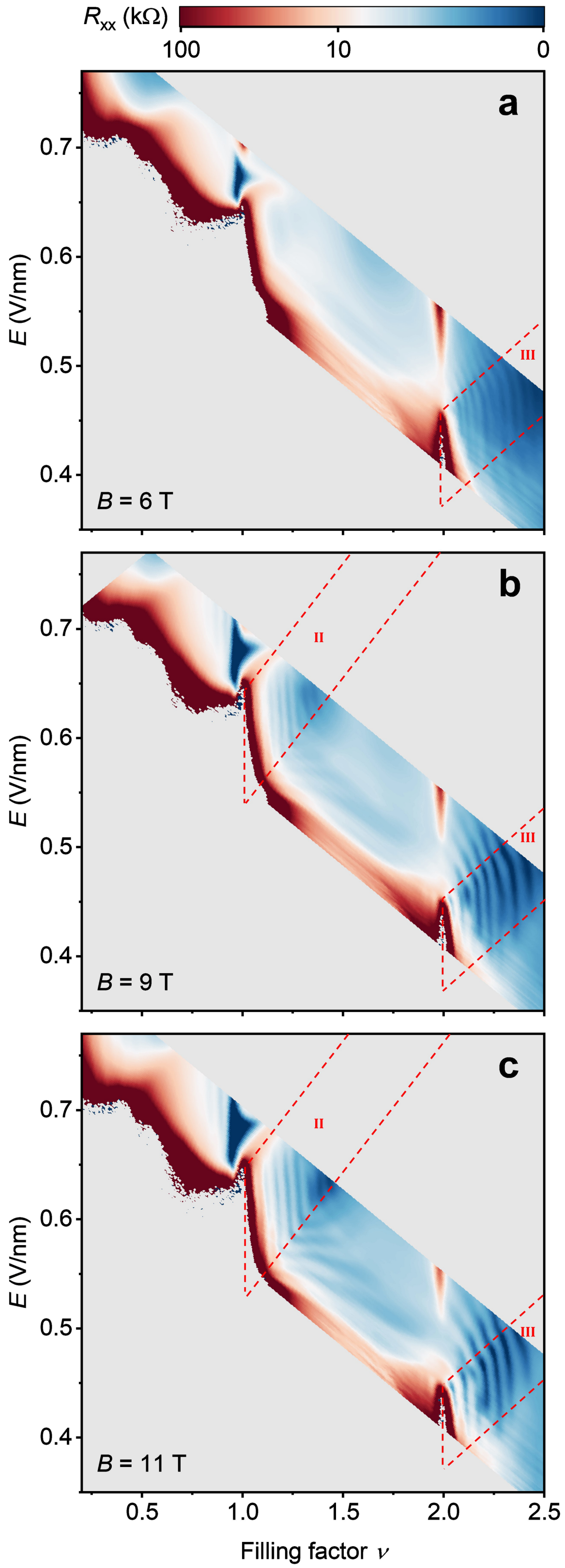

Extended Data Fig. 2 | Filling factor and electric field dependent R_{xx} at different magnetic fields. a, b, c, Dependence of R_{xx} on the total filling factor ν and the out-of-plane electric field E at $T = 1.6$ K and $B = 6$ T (**a**), 9 T (**b**) and 11 T (**c**). The dashed lines mark the phase boundaries for region II and III. Region II cannot be identified at $B = 6$ T without Landau levels. The electric field span expands (shrinks) for region II (III) with increasing B.

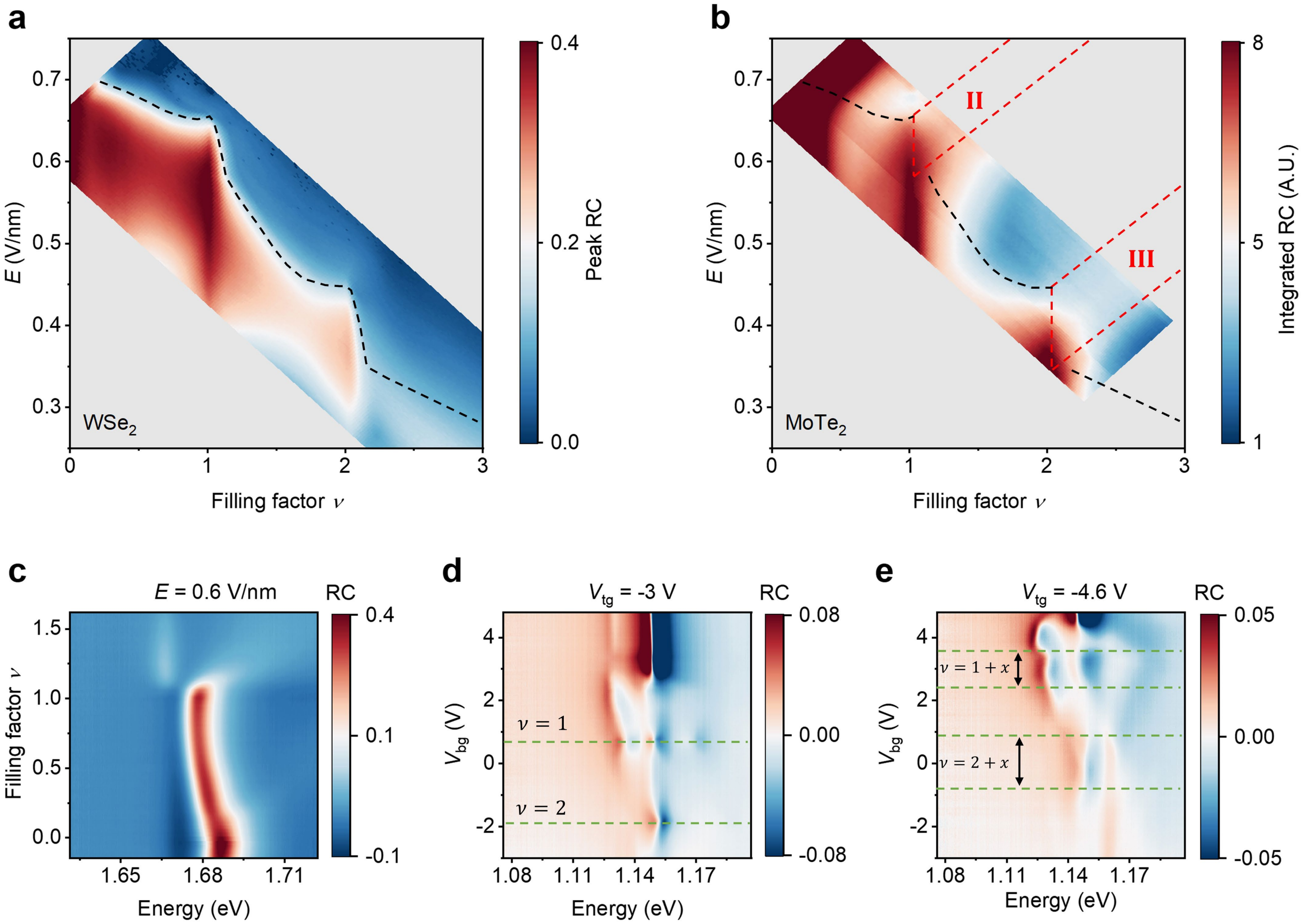

Extended Data Fig. 3 | Filling factor and electric field dependence of exciton reflection contrast. a, b, The reflection contrast (RC) for the intralayer exciton resonance of WSe_2 (**a**) and $MoTe_2$ (**b**) as a function of filling factor and electric field at $B = 0$ T and $T = 1.6$ K. The peak RC and the spectrally integrated RC (over the exciton resonance) are shown in **a** and **b**, respectively. **c**, Filling factor dependence of the RC spectrum near the WSe_2 exciton resonance at $E = 0.6$ V/nm. The much weakened neutral exciton resonance accompanied by the appearance of the Fermi polaron resonances for $\nu > 1$ shows that the WSe_2 layer is hole-doped above $\nu = 1$. Repeated measurements at varying electric fields construct the full map in **a**. The sharp drop in the exciton RC with doping helps construct the black dashed line in **a**, above which WSe_2 is hole-doped. **d**, **e**, Bottom gate voltage (V_{bg}) dependence of the RC spectrum near the $MoTe_2$ exciton resonance at top gate voltages $V_{tg} = -3$ V (**d**) and $V_{tg} = -4.6$ V (**e**). While holes are only doped into the $MoTe_2$ layer in **d**, holes are shared between the two TMD layers in **e**. Similar to WSe_2, the neutral exciton resonance (near 1.14 eV) is weakened substantially when $MoTe_2$ is hole-doped (e.g., near $V_{bg} = 3$ V in **d**). The charged exciton resonance is enhanced at the insulating states at $\nu = 1$ and 2 (e.g., green dashed lines in **d**). Multiple moiré exciton resonances are also observed near $\nu = 1$. Similar results are also observed in **e** except now the WSe_2 layer also becomes hole-doped. As a result, there is an extended span in V_{bg} (bound by the green dashed lines and indicated by the arrows) that the $MoTe_2$ layer is kept in an insulating state (Mott insulator for $\nu = 1 + x$ and moiré band insulator for $\nu = 2 + x$). Repeating the measurements in **d** and **e** at varying V_{tg} constructs the full map in **b**. The extended regions bound by the green dashed lines in **e** together with the black dashed line in **a** help identify region II and III in **b**.

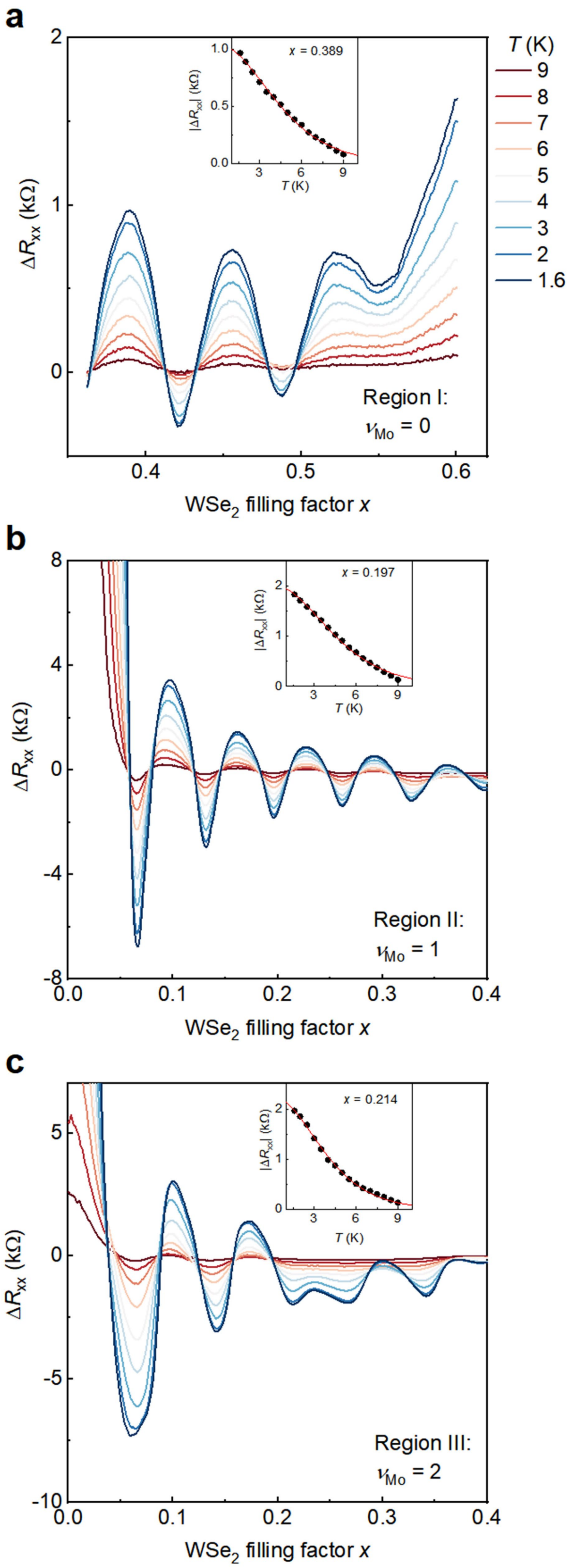

Extended Data Fig. 4 | Determination of the WSe_2 hole mass from quantum oscillations. a, **b**, **c**, Temperature dependence of the quantum oscillation amplitude ΔR_{xx} as a function of ν_W at $B = 13.6$ T for region I (**a**), II (**b**), III (**c**). The filling factor dependence of R_{xx} at $T = 10$ K, where there is no quantum oscillation, is used as a background to obtain ΔR_{xx}. The insets show the fits of $|\Delta R_{xx}|$ versus T to $\Delta R_{xx} = R_{a}\frac{\lambda(T)}{\sinh\lambda(T)}$ in order to obtain the mass m_W. Here R_a is the amplitude and the thermal factor is $\lambda(T) = 2\pi^2 k_B T m_W/\hbar eB$ (k_B denotes the Boltzmann constant).

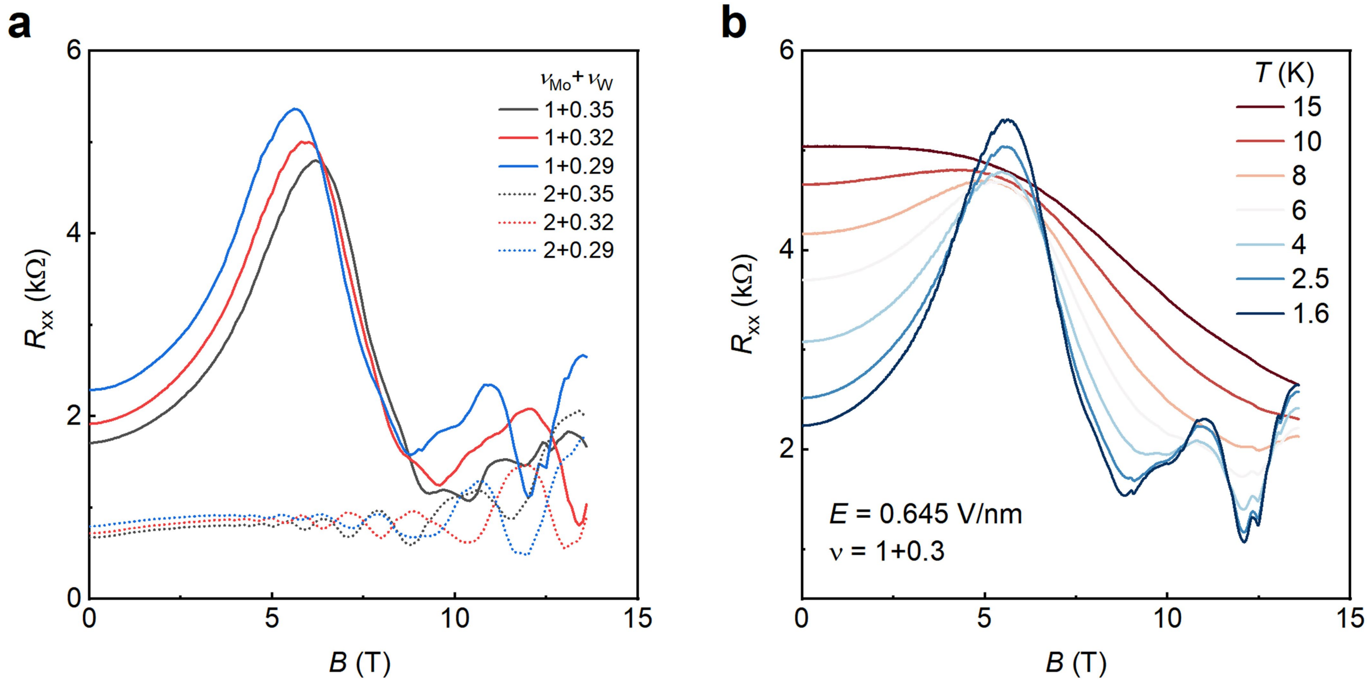

Extended Data Fig. 5 | Additional data on magnetic destruction of Kondo singlets. **a**, Magnetic field dependence of R_{xx} at $T = 1.6$ K in region II (solid curves) and III (dotted curves). Whereas a small magnetoresistance is observed in region III (except the quantum oscillations at high fields), a large, quadratic magnetoresistance is observed in region II before the magnetic destruction near 6 T. R_{xx} for the two regions become comparable after the magnetic destruction. **b**, Magnetic field dependence of R_{xx} at different temperatures in region II. The temperature dependence corresponds to that in Fig. 3f for R_H.

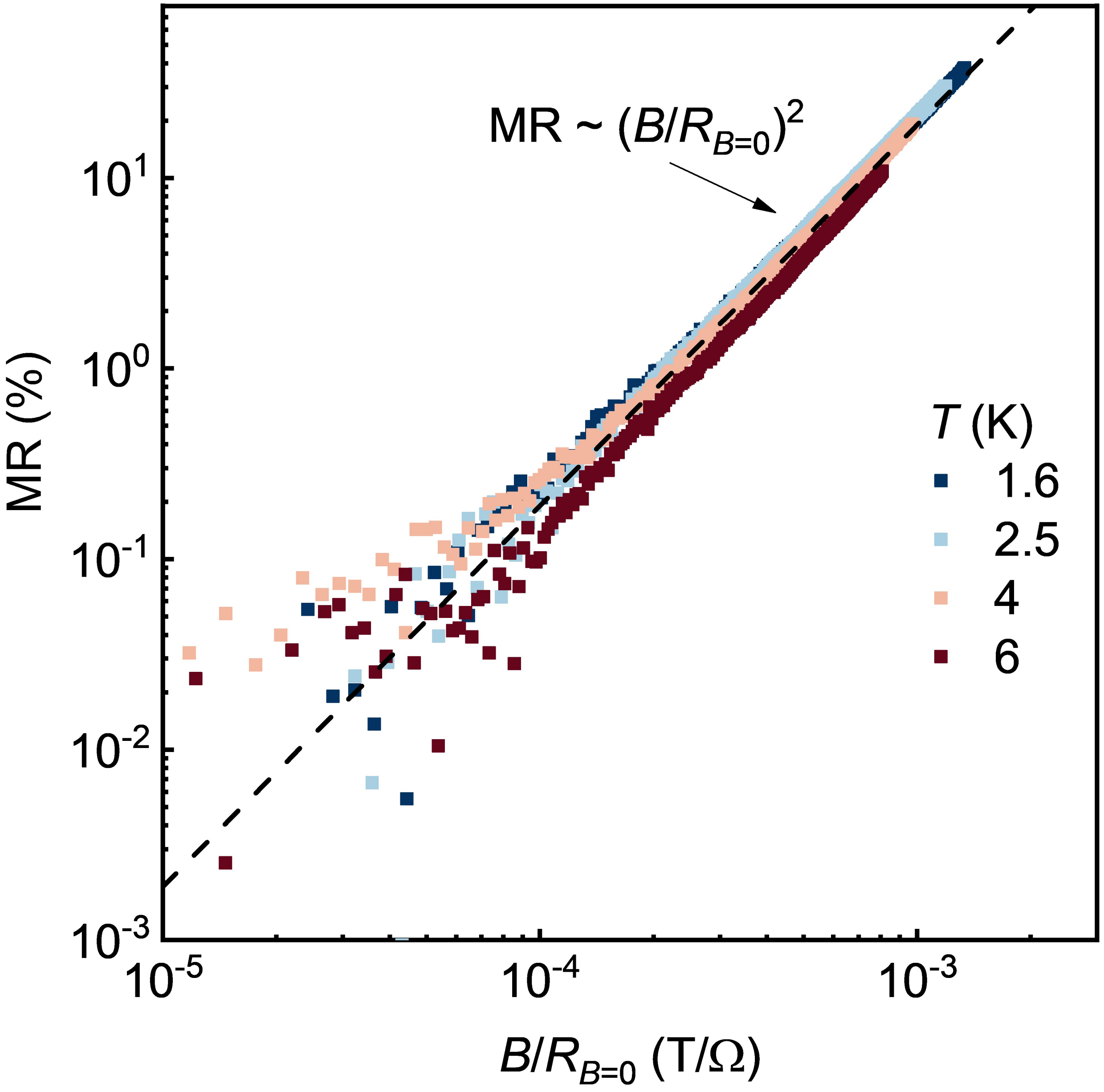

Extended Data Fig. 6 | Kohler's scaling in region II. Magnetoresistance (MR) as a function of the scaled magnetic field (by the zero-field $R_{xx} \equiv R_{B=0}$) at $\nu = 1 + 0.3$ and varying temperatures. All curves collapse to the trend $MR \propto \left(\frac{B}{R_{B=0}}\right)^2$ as shown by the black dashed line. The data further confirms the Fermi liquid behavior in region II.

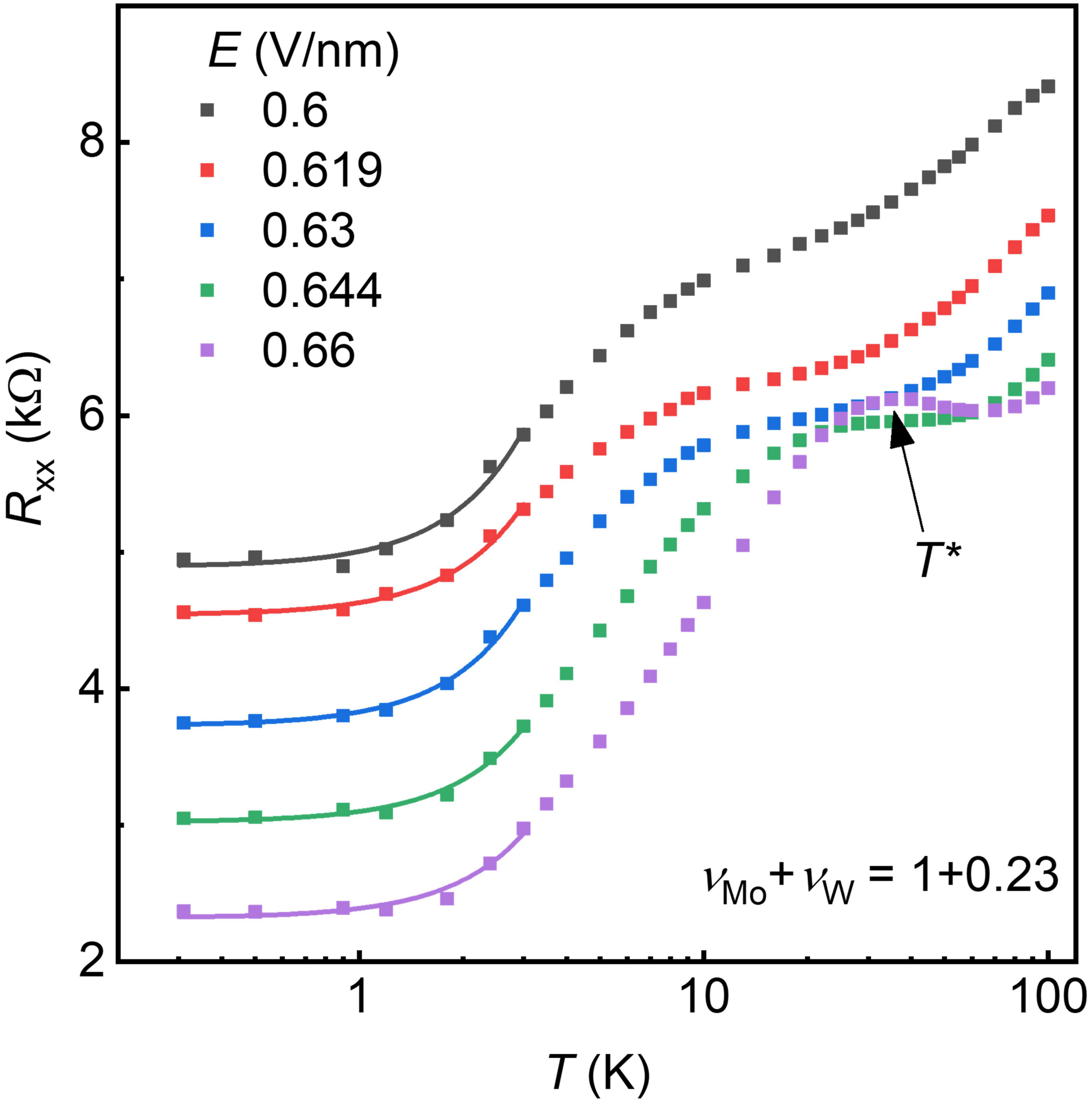

Extended Data Fig. 7 | Temperature dependence of R_{xx} at varying electric field in region II. The solid lines are the best fits to the quadratic temperature dependence at low temperatures. The resistance peak/bump determines the Kondo temperature T^*.

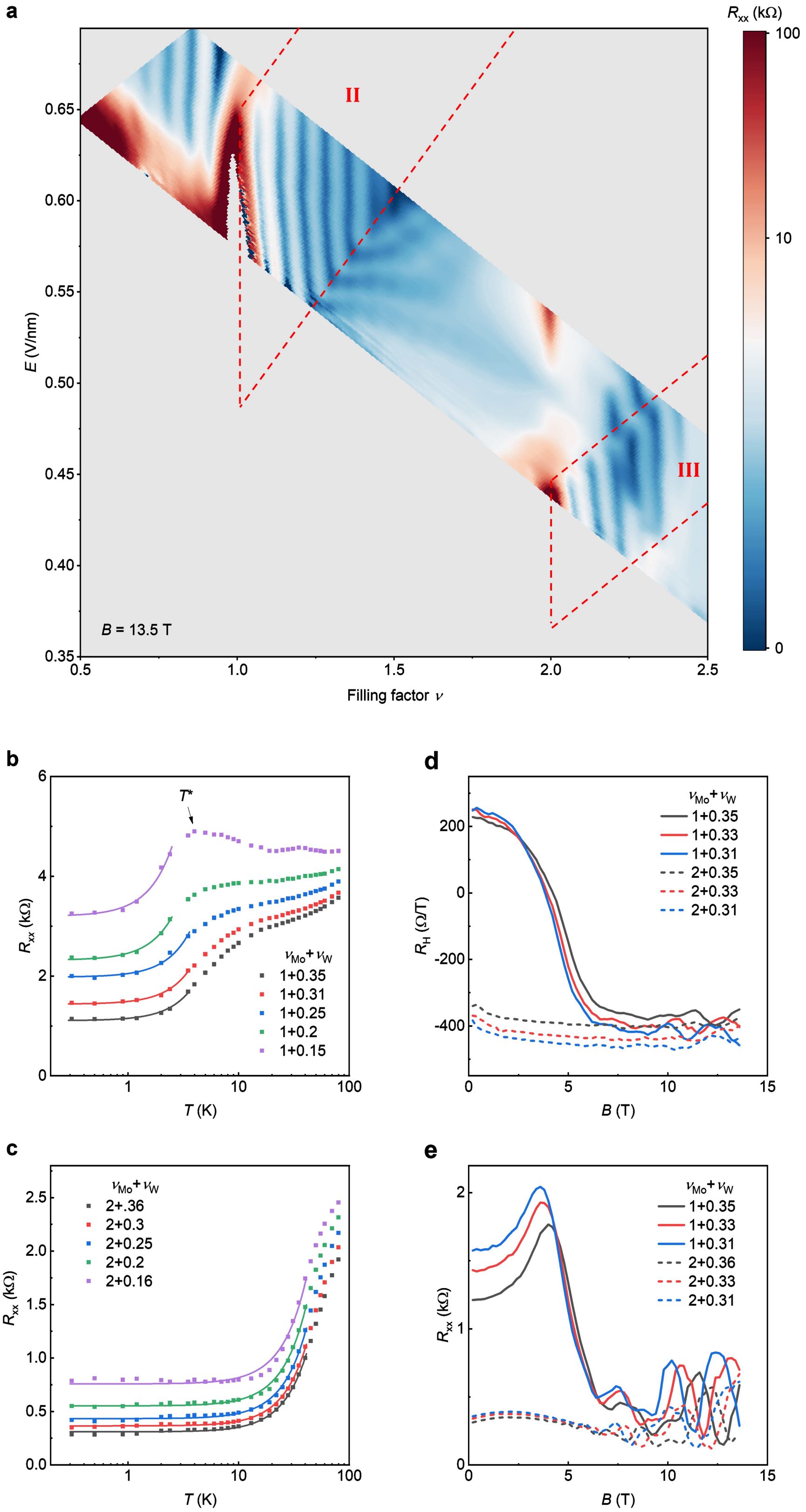

Extended Data Fig. 8 | Reproducible results in device 2. a, Dependence of R_{xx} on ν and E at $B = 13.5$ T and $T = 1.6$ K. The red dashed lines mark the boundaries of region II and III. **b, c**, Temperature dependence of R_{xx} at varying doping densities for $\nu = 1 + x$ (**b**) and $\nu = 2 + x$ (**c**). The solid lines are the best fits to the quadratic temperature dependence at low temperatures. **d, e**, Magnetic field dependence of R_H (**d**) and R_{xx} (**e**) at $T = 1.6$ K for both $\nu = 1 + x$ (solid curves) and $\nu = 2 + x$ (dashed curves). A sharp change in R_H at the critical magnetic field is observed only for $\nu = 1 + x$; that at $\nu = 2 + x$ is nearly field independent.

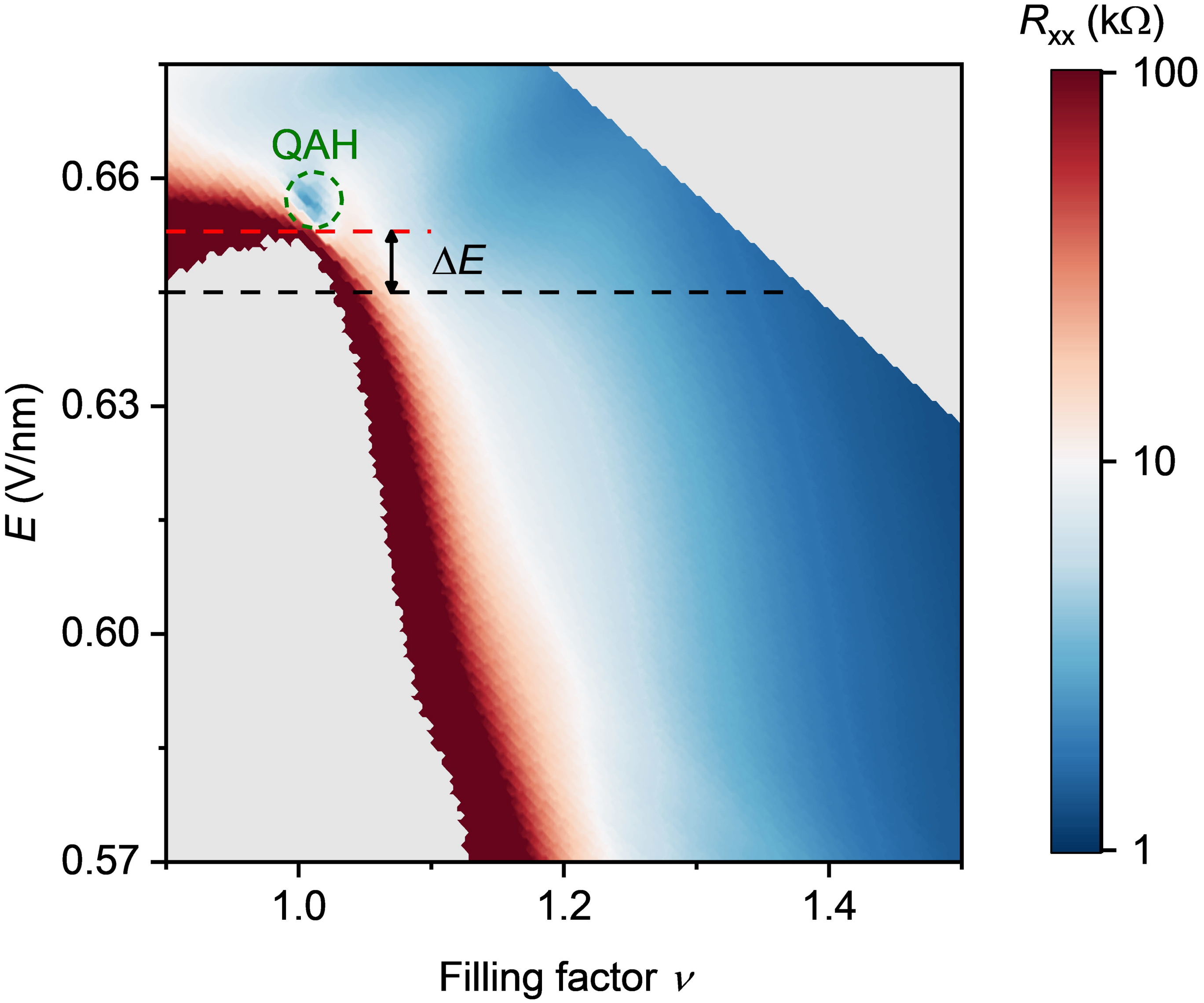

Extended Data Fig. 9 | Determination of the charge transfer gap. Dependence of R_{xx} on the total filling factor ν and out-of-plane electric field E at $B = 0$ and $T = 1.6$ K. The green dashed circle marks the region for the quantum anomalous Hall (QAH) insulator. The critical electric field for band inversion at $\nu = 1$ is marked by the red dashed line at $E = 0.653$ V/nm. The black dashed line shows the electric field ($E = 0.645$ V/nm) at which the data in Fig. 3 were taken. The charge transfer gap is given by the product of the interlayer dipole moment and the electric field difference ΔE.

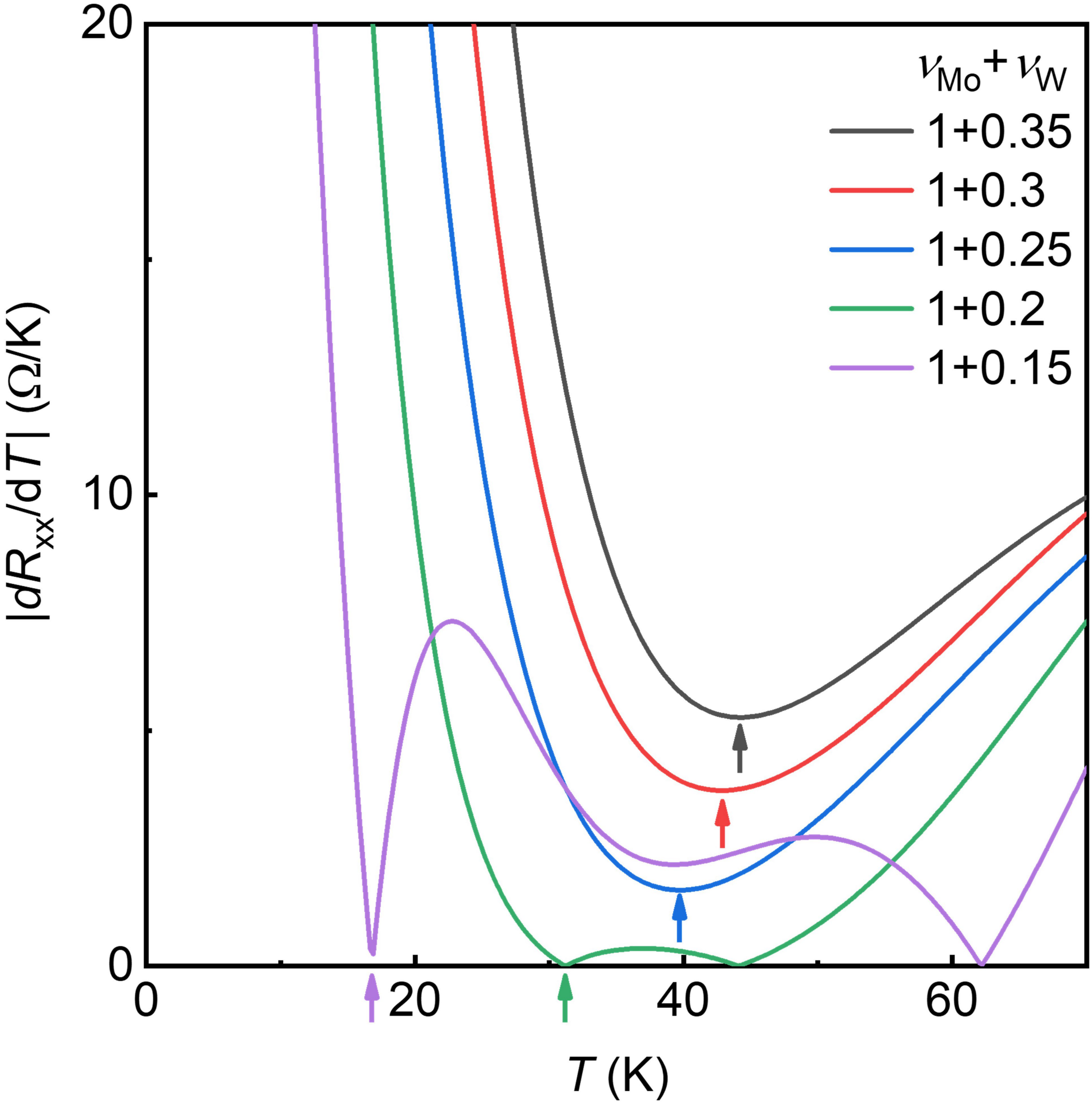

Extended Data Fig. 10 | Temperature dependence of $|dR_{xx}/dT|$ at varying WSe$_2$ filling factor x. The data were extracted by first smoothing the experimental temperature dependence of R_{xx} before taking numerical derivatives. The temperature T^* is determined by the first minimum of $|dR_{xx}/dT|$ (marked by arrows).